Dalton
Transactions

ROYAL SOCIETY
OF CHEMISTRY

PAPER

View Article Online
View Journal

Check for updates

Cite this: DOI: 10.1039/d6dt00551a

Rational design of BODIPY-functionalized MOF photocatalysts for highly efficient hydrogen production

Zehra Coşkun,[a] Elif Yıldız Gül,[a,b] Burcu Topaloğlu Aksoy,[a] Azam Seifi,[c]
Esra Tanrıverdi Eçik[b] and Bünyemin Çoşut *[a]

Received 6th March 2026,
Accepted 12th May 2026

DOI: 10.1039/d6dt00551a

rsc.li/dalton

Photocatalytic hydrogen production through water reduction, driven by hydrogen's high energy density and environmental sustainability, represents a significant pathway for meeting future energy needs and is considered one of the most promising strategies. A major challenge is developing a photocatalyst that is sustainable, stable, and environmentally friendly and has a large surface area. Although various MOF-based photocatalysts incorporating porphyrins, phthalocyanines, or other organic dyes have been extensively explored, studies utilizing BODIPY as a functional chromophore remain scarce. The combination of MOFs with BODIPY units offers a unique platform that couples the structural tunability and stability of MOFs with the excellent light-harvesting and electron-accepting properties of the BODIPY dyes. However, strategies for the systematic design and synthesis of BODIPY–MOF hybrid photocatalysts for hydrogen evolution are still very limited. In this study, the UiO-66-NH_2 structure was modified with BODIPY compounds containing thiophene (BD2) and phenyl (BD4) units, resulting in the synthesis of BD2/UiO-66-NH_2 and BD4/UiO-66-NH_2, respectively. As a result of the 6-hour photocatalytic water splitting experiments, the reaction kinetics of UiO-66-NH_2, BD2/UiO-66-NH_2, and BD4/UiO-66-NH_2 were calculated to be 3013 μmol g^{-1} h^{-1}, 14 237 μmol g^{-1} h^{-1} (4.7-fold increase compared to UiO-66-NH_2), and 21 179 μmol g^{-1} h^{-1} (7-fold increase compared to UiO-66-NH_2), respectively. Based on the band structure and photoelectrochemical results, the observed behavior is consistent with the S-scheme charge-transfer pathway for the photocatalytic process. This study provides new insights into integrating BODIPY chromophores into MOF frameworks, establishing a promising design concept for the development of efficient dye–MOF hybrid photocatalysts for solar-to-hydrogen conversion.

1. Introduction

The growing worldwide energy requirement, in parallel with the environmental consequences of fossil fuel consumption, has intensified the pursuit towards sustainable and low-carbon energy alternatives. Sustainability-oriented energy systems that rely on renewable energy sources such as solar, hydro, wind, and geothermal energies offer long-term solutions due to their inherent renewability and minimal environmental footprint.[1] Among these, solar energy is particularly attractive owing to its abundance, wide geographic availability, and potential for direct conversion to chemical fuels. In this context, solar-driven hydrogen evolution *via* photocatalytic water splitting has developed into a viable approach for sustainable fuel generation as it enables the direct utilization of sunlight to produce hydrogen without carbon emissions. This strategy not only addresses the intermittency of solar power by enabling energy storage in a chemical form but also aligns with global efforts to establish a carbon-neutral hydrogen economy.[2,3]

Photocatalysis offers an applicable approach for converting solar energy into chemical fuels through light-driven redox reactions.[4] In particular, photocatalytic water splitting has gained significant attention as a sustainable method for hydrogen generation, relying on semiconductor materials to harvest photons and facilitating the overall water-splitting reaction.[5] Upon irradiation with light of appropriate energy, these materials generate electron–hole pairs that can drive the reduction of protons to H_2 and the oxidation of H_2O to O_2. However, the practical efficiency of photocatalytic systems remains limited by several factors, including rapid charge recombination, limited visible-light absorption, and poor stability under reaction conditions.[6–8] To overcome these challenges, considerable research has been focused on the rational design of photocatalysts with modified band structures,

---

[a] Department of Chemistry, Gebze Technical University, 41400 Gebze, Türkiye. E-mail: bcosut@gtu.edu.tr; Fax: +90 262 6053105; Tel: +90 262 6053015
[b] Department of Chemistry, Atatürk University, 25240 Erzurum, Türkiye
[c] Department of Environmental Engineering, Kocaeli University, Türkiye

extended light-harvesting capabilities, and efficient charge-separation pathways. The integration of molecular photosensitizers, cocatalysts, and porous architecture has proven particularly effective in improving the photocatalytic performance and durability of these systems under solar irradiation.[9,10]

Among the emerging classes of organic photosensitizers, BODIPY (boron dipyrromethene) dyes are fluorescent dyes that have excellent photophysical characteristics, such as sharp absorption bands, elevated fluorescence quantum yields, high molar absorption coefficients, long-lived excited triplet state, and thermal/photochemical stability.[11] Owing to their tunable photophysical behavior and efficient light-harvesting characteristics, BODIPY derivatives have been employed as effective photosensitizers in a variety of photocatalytic applications, including photoorganic transformations[12] and photocatalytic hydrogen evolution.[13,14] Their highly conjugated and structurally rigid frameworks enable precise modulation of electronic transitions, facilitating strong visible-light absorption and efficient energy transfer within hybrid photocatalytic systems.

Parallel to these advancements, porous crystalline materials, like metal–organic frameworks (MOFs), have come out as a versatile platform for designing next-generation photocatalysts.[15] While certain frameworks exhibit semiconducting behavior due to optimized charge-transfer pathways between the metal centers and ligands, their electronic properties are highly dependent on the nature of the coordination environment.[16,17] The positively charged inorganic nodes, typically metal ions or clusters, and anionic/neutral organic ligands are the building blocks of MOF structures.[18] To form the framework structure, building blocks are linked with coordination covalent bonds. This type of material has a crystalline polymeric structure with regularly repeating units and can be obtained by connecting organic structural units *via* covalent bonds.[17] Since MOF structures have a high surface area, functionalized crystalline and controllable structure, and tunable band gap, they have been chosen for photocatalytic hydrogen production applications.[17,19–23] The ultra-high porous structure and thermal and chemical stability of MOFs are some of the important features for considering them as catalyst candidates.[18] The pore surface and size of MOF structures allow them to be functionalized with organic linkers, and this approach is considered advantageous for hydrogen evolution applications.[18,24] In the catalysis area, attention to MOF structures is increasing due to their versatile solid-state platform for heterogeneous, stable, and single-state catalysis. Especially in hydrogen evolution reactions, their stability under catalytic conditions is an important factor, and a large number of MOFs show water stability.[24]

Considering the above-mentioned points, the application of photocatalysts like MOFs, which are engineered with BODIPY-based photosensitizers, can enhance the efficiency of hydrogen production *via* photocatalytic processes. The main focus of the present study is the preparation of porous MOFs with tunable pore sizes using BODIPY-based photosensitizers possessing strong photonic properties, and the investigation of the photocatalytic hydrogen-production potential of the synthesized structures. To date, the physicochemical properties of BODIPY–MOFs, such as specific surface area, conjugated structure, visible light absorption ability, band gap configuration, charge separation, and transfer, responsible for the elevated photocatalytic performance have not been fully investigated in the literature. Although luminescent MOFs have been reported in the literature, BODIPY-based emissive MOFs have rarely been documented,[25–27] and their numbers are significantly limited compared to other types of MOFs. Moreover, it is known that fundamental uncertainties remain in the mechanisms of MOF-based photocatalytic systems. With this study, a systematic investigation of the photocatalytic processes of BODIPY-based MOF structures was conducted (Scheme 1), contributing to the existing literature. As a result of the planned design details, not only new, stable MOFs with high photocatalytic efficiency were developed but also a systematic investigation was carried out to address uncertainties in the fundamental mechanisms of MOF-based photocatalytic systems, thereby filling a significant gap in the literature.

2. Results and discussion

BODIPY derivatives carrying a formyl group at the β-position were designed as fluorophore groups for post-modifications of UiO-66-NH_2. These compounds were synthesized as depicted in Scheme S1. First, the classical BODIPY synthesis protocol was followed using 3-thiophenecarboxaldehyde or benzaldehyde and 2,4-dimethylpyrrole in the presence of TFA. After *p*-chloranil was added, the mixture was treated with triethylamine (Et_3N) and boron trifluoride diethyl etherate to give BD1 and BD3. The Vilsmeier–Haack reactions of BD1 and BD3 using phosphoryl chloride and DMF were carried out to yield β-formyl BODIPYs BD2 and BD4. The yields of BD2 and BD4 obtained from the Vilsmeier–Haack reactions were 65% and 95%, respectively. The structures of BD2 and BD4 were verified by mass spectrometry and ^1H and ^{13}C NMR spectroscopic techniques. The mass spectrum of BD4 gave a molecular ion peak at m/z 352.042 and another peak at m/z 333.023, resulting from the loss of a fluorine atom. The ^1H NMR spectra of BD2 and BD4 exhibited proton signals from the formyl groups at approximately 10 ppm. Aromatic proton signals of BD2 and BD4 were observed at 7.5–6.1 ppm, while the signals at 2.8–1.5 ppm were assigned as methyl proton signals.

To assess the crystalline structure preservation of the composite materials, PXRD patterns of pure UiO-66-NH_2 and BODIPY-functionalized MOFs containing BD2 and BD4 were obtained and compared with the simulated UiO-66-NH_2 pattern (Fig. 1A). Characteristic diffraction peaks for UiO-66-NH_2 at 2θ = 7.4°, 8.5°, 12°, and 25.7° were observed, which were consistent with the simulations, confirming the successful synthesis and high crystallinity of the material. These characteristic peaks are highly preserved in both BD2/UiO-66-NH_2 and BD4/UiO-66-NH_2, indicating that the crystalline framework remains intact despite the integration of the BD2 and BD4 into the MOF structure. The slight decrease in peak

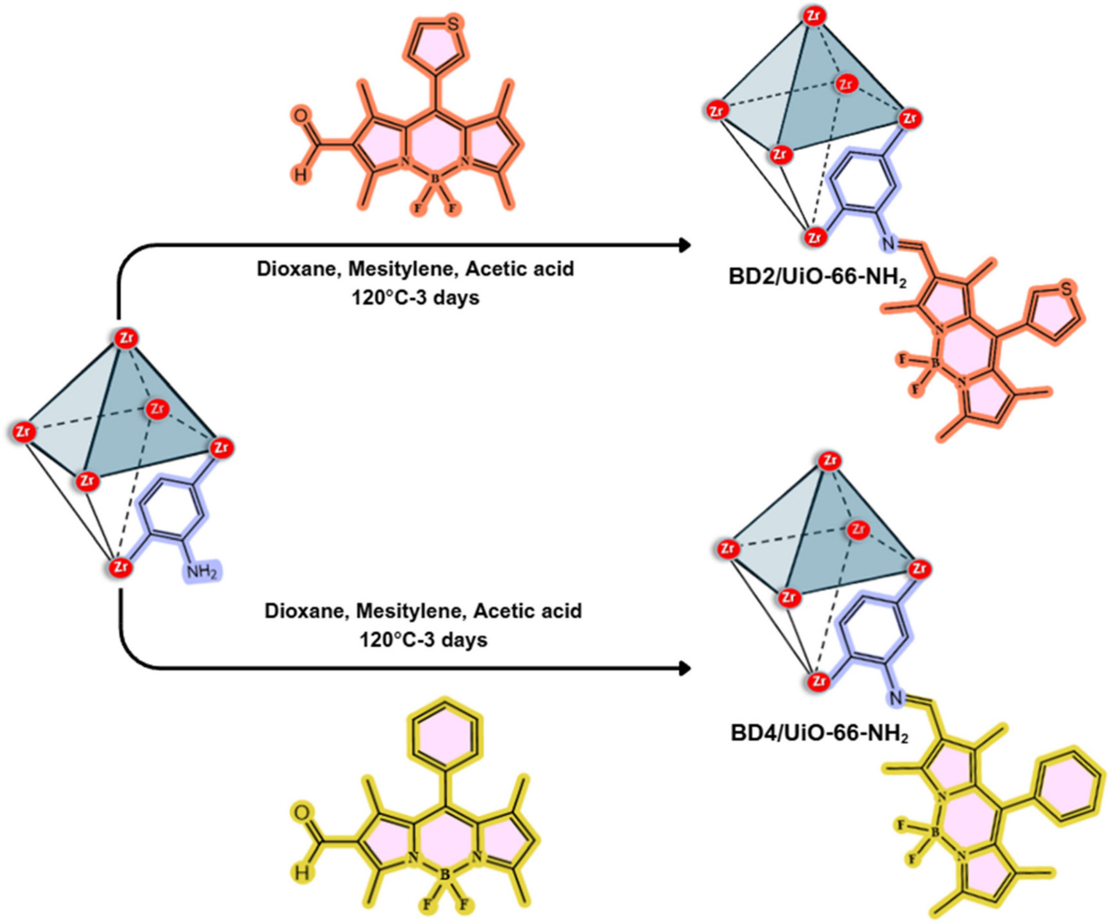

Scheme 1 Synthetic routes to BODIPY-functionalized MOF structures.

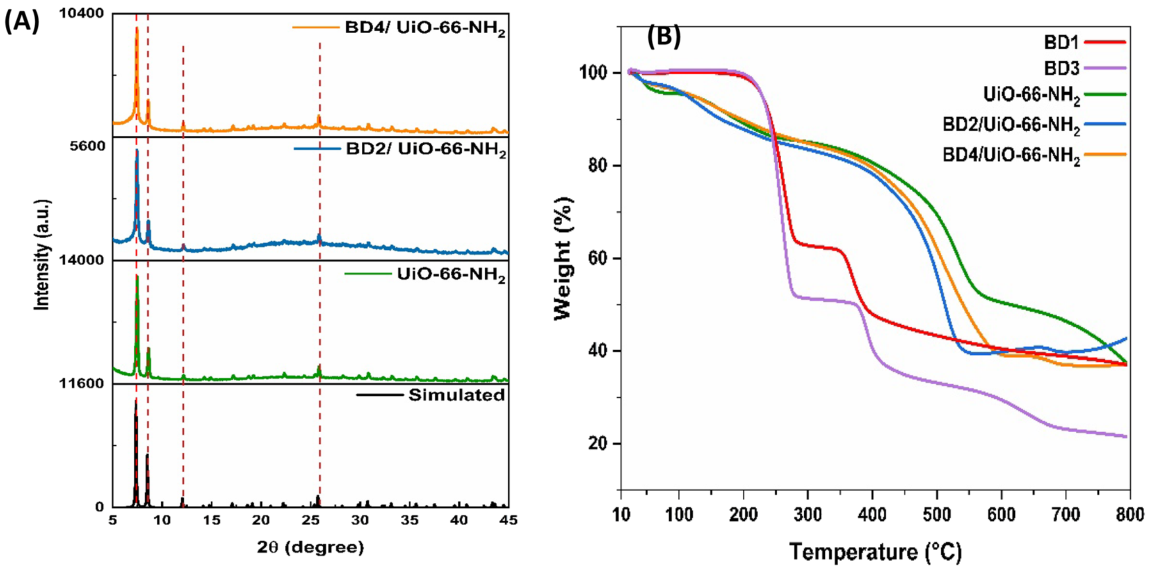

Fig. 1 BODIPY-functionalized MOFs: (A) PXRD patterns and (B) TGA thermograms.

intensities following functionalization suggests that the pores are occupied by BODIPY molecules.[28] As seen in the PXRD pattern, peak broadening was observed for BD2/UiO-66-NH_2 and BD4/UiO-66-NH_2. The crystallite sizes of UiO-66-NH_2, BD2/UiO-66-NH_2, and BD4/UiO-66-NH_2 were determined to be 36.8 nm, 24.7 nm, and 30.7 nm, respectively, using the Scherrer relationship ($D = K\lambda/\beta\cos\theta$), where K is the shape constant (0,9), λ is the wavelength of the incident X-ray beam, and β is the full width at half maximum of peaks (in radians); $\beta\cos\theta$ corresponds to the peak broadening of a diffraction peak. BD2/UiO-66-NH_2 exhibited a smaller crystallite size compared to UiO-66-NH_2 and BD4/UiO-66-NH_2, which can be attributed to the inverse relationship between crystallite size and peak broadening, evaluated from the full width at half maximum (FWHM).[29,30]

The FT-IR spectra of UiO-66-NH_2 and its composites contain characteristic peaks that confirm the presence of functional groups in these structures (Fig. S12). The peaks detected at 3471 cm^{-1} and 3365 cm^{-1} in the spectrum of UiO-66-NH_2 are associated with the asymmetric and symmetric N–H stretching vibrations of the primary amine (–NH_2) groups, respectively, that were efficiently introduced into the structure. The 1566 cm^{-1} band represents the asymmetric C=O stretching vibrations of the carboxylate groups, while the peak at 1384 cm^{-1} represents the symmetric C–O stretching vibrations. The peak at 1259 cm^{-1} is associated with the C–N stretching vibrations attached to the aromatic ring, indicating that the amine functional group is retained in the ligand. In the low-wavenumber region, the peak at 659 cm^{-1} is associated with metal–oxygen vibrations, indicating the presence of Zr–O–C bonds. These data support coordination of 2-aminoterephthalic acid with the Zr^{4+} unit and the synthesis of the UiO-66-NH_2 structure. Fig. S12A illustrates the FTIR spectra of BD2/UiO-66-NH_2 and its starting materials, and Fig. S12B represents the FTIR spectra of BD4/UiO-66-NH_2 and its starting materials. When these spectra are evaluated, there is a decrease in the intensity of the primary amine vibration peaks located around 3300 cm^{-1} for both composites, which is thought to be due to the reaction of the amine groups of UiO-66-NH_2 with the aldehyde groups of B2 and BD4.

TGA results in Fig. 1B indicate that pure BD1 and BD3 decompose rapidly at low temperatures. BD1 lost approximately 62.9% of its mass, while BD3 lost approximately 78.5%. This suggests that BD1 and BD3 are thermally unstable and cannot withstand high temperatures. Pure UiO-66-NH_2 lost approximately 62.4% of its mass in the range of 300–550 °C. Decomposition began at higher temperatures and progressed more slowly than for the BODIPYs. This suggests that UiO-66-NH_2 is structurally more stable. Two-stage degradation was observed in the BD2/UiO-66-NH_2 and BD4/UiO-66-NH_2. In the first stage, mass loss occurred between 100 and 150 °C, which was attributed to the removal of water or solvents from the pores. In the second stage, mass loss ranged between 250 and 550 °C. BD2/UiO-66-NH_2 and BD4/UiO-66-NH_2 exhibit greater thermal stability at elevated temperatures compared to BD1 and BD3.

The surface chemical environment and elemental composition of the BD4/UiO-66-NH_2 composite (which showed the best performance in H_2 evolution, according to the obtained results reported in Fig. 7) were examined by XPS. The high-resolution spectra of the C 1s, O 1s, N 1s, F 1s, and Zr 3d regions verify the coexistence of both the MOF framework and the BODIPY dye and provide direct evidence for the successful conjugation of the dye onto the amine-functionalized UiO-66 structure. The C 1s spectrum (Fig. 2A) is deconvoluted into four characteristic components. The dominant peak at ~283.9 eV corresponds to the C–C/C–H species structure. A secondary feature at ~284.6 eV is attributed to C=C groups associated with the conjugated aromatic system present in both components. The peak centered at ~285.1 eV is assigned to C–N bonds, confirming the presence of the amine-functionalized linker and the nitrogen-containing moieties within the BODIPY core. The higher-binding-energy contribution at ~288.2 eV is associated with the O–C=O groups of coordinated carboxylates bound to the Zr_6 clusters. The combined features of the C 1s spectrum indicate that both the UiO-66-NH_2 linker and the BODIPY molecules remain chemically intact following conjugation. The O 1s spectrum (Fig. 2B) presents two well-defined components. The lower-binding-energy peak at ~531.2 eV corresponds to the lattice oxygen within the Zr–O coordination environment. In comparison, the higher-binding-energy peak at ~533.4 eV is attributed to carbonyl oxygen originating from coordinated carboxylates and oxygen-containing groups of the structure. The preservation of the lattice O–Zr signal demonstrates that the Zr-based secondary building units retain their structural integrity after dye attachment. The N 1s spectrum (Fig. 2C) offers compelling evidence for the successful incorporation of BODIPY into the MOF. The peak at ~398.2 eV corresponds to the N–C bonds of the composite. A distinct additional feature at ~400.2 eV is assigned to the N–B bond, which is a fingerprint of BODIPY dyes. The F 1s spectrum (Fig. 2D) displays a characteristic peak at approximately 684.9 eV, corresponding to the F–B groups intrinsic to the BODIPY structure. The Zr 3d region (Fig. 2E) exhibits the typical spin–orbit doublet of Zr^{4+} species, with Zr $3d_{5/2}$ and Zr $3d_{3/2}$ located at ~182.2 and ~184.6 eV, respectively. These results are in agreement with the previously reported values for UiO-type MOFs and indicate that the local coordination environment around the Zr_6 clusters remains unchanged upon functionalization.

SEM images were recorded to examine the morphological structures, as shown in Fig. 3A–C. It was revealed that functionalization of UiO-66-NH_2 *via* the Schiff base reaction significantly altered the surface properties of the MOF while maintaining its cubic morphology. While regular cubic shapes were observed before modification, the cubic morphology was preserved in BD2/UiO-66-NH_2 and BD4/UiO-66-NH_2. However, surface roughness increased, and the particle size increased from 181 nm to 225 nm and 192 nm, respectively (Fig. 3D–F). These results indicated that post-synthetic functionalization altered the surface topography without disrupting the morphological shape.

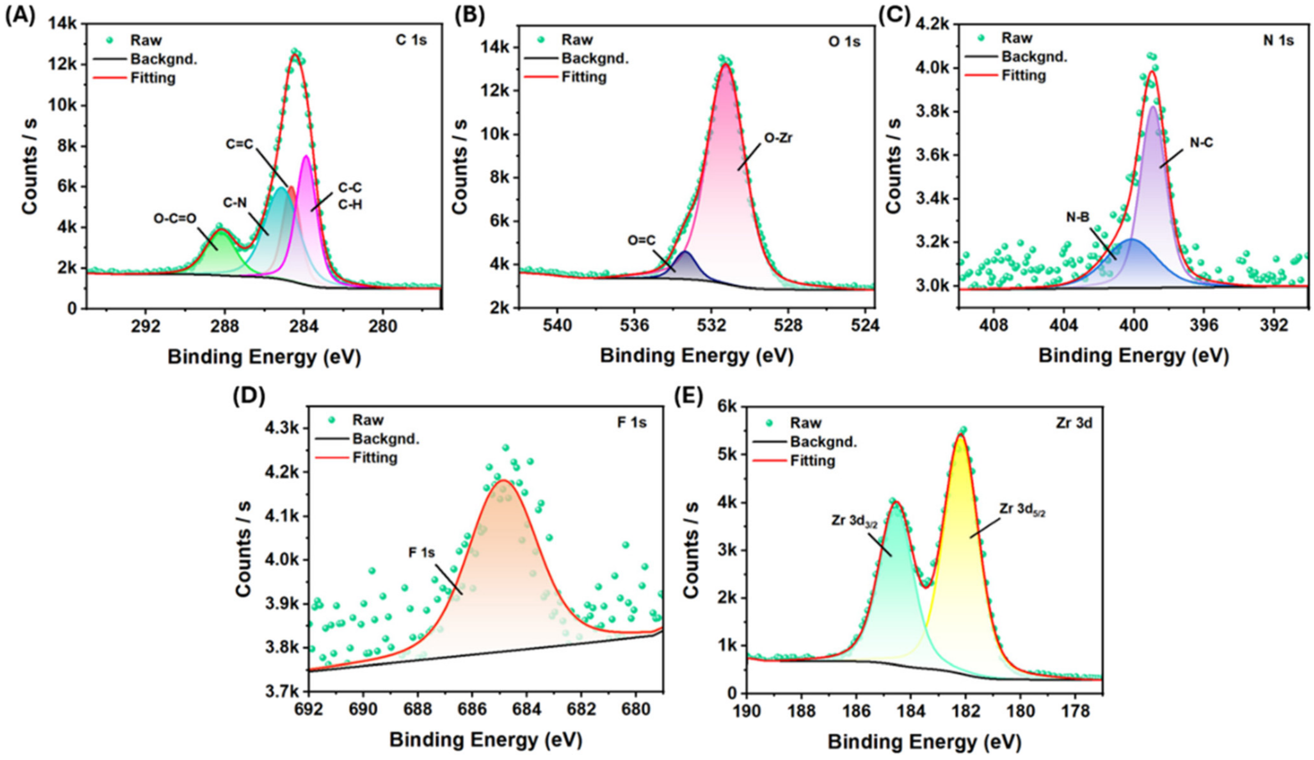

Fig. 2 High-resolution XPS spectra of (A) C 1s, (B) O 1s, (C) N 1s, (D) F 1s, and (E) Zr 3d of BD4/UiO-66-NH_2.

EDS analysis was employed to identify the elemental constituents of the synthesized compounds (Fig. 3G–I). The EDS analysis revealed that the products obtained were consistent with their main components.

Fig. 4 reveals the TEM images of UiO-66-NH_2 and BD4/UiO-66-NH_2. The TEM image in Fig. 4A clearly demonstrates the distinct and smooth cubic crystal morphology of bare UiO-66-NH_2. In contrast, the TEM image of BD4/UiO-66-NH_2 (Fig. 4B and C) reveals that the cubic structure is generally preserved, but the surface acquires a rougher and more heterogeneous appearance. TEM images of UiO-66-NH_2 and BD4/UiO-66-NH_2 at different magnifications are given in Fig. S13 and S14, respectively. This surface change indicates that the BODIPY groups have been successfully bonded to the MOF structure *via* the Schiff base bond. This confirms the effective integration of BODIPY onto the MOF surface. The evolution of the pore architecture was quantitatively monitored through BET surface area analyses for both pristine MOF and after post-modification with BODIPY BD4; the related results are shared as SI. The pristine UiO-66-NH_2 sample exhibited a high specific surface area of 1210.3 m^2 g^{-1}, confirming its characteristic microporous nature. Following the post-synthetic modification strategy, a sharp and consistent decrease in the BET surface area to 657.6 m^2 g^{-1} was observed, providing direct evidence of the successful integration of functional units into the framework. This reduction in surface area is primarily attributed to the partial occupancy of the pore cavities by the newly introduced bulky groups, which create steric hindrance and subsequently restrict the accessible space for nitrogen (N_2) molecules.

Fig. 5A shows the Tauc plots that were constructed to determine the optical band gaps of UiO-66-NH_2, BD2/UiO-66-NH_2, and BD4/UiO-66-NH_2 using the absorbance and reflectance spectra in Fig. S15–S17. The analysis revealed band gaps of 2.84 eV, 2.04 eV, and 2.05 eV, respectively. The obtained values demonstrate that the materials have semiconducting properties and are active in the visible-light region. The addition of BODIPY structures to bare UiO-66-NH_2 significantly reduced the optical band gap. Fig. 5B shows the Mott–Schottky plot of the bare UiO-66-NH_2, BD2/UiO-66-NH_2, and BD4/UiO-66-NH_2. The positive slope of the obtained plots proves that the bare and doped MOF structures are n-type semiconductors, with corresponding flat band potentials (V_{FB}) of −1.16, −1.06, and −1.05 V (*vs.* Ag/AgCl reference electrode), respectively. Considering the following conversion formulas for obtaining the conduction band potential, E_{CB} (eqn (1) and (2)), and the equation used for the band gap calculation ($E_g = E_{VB} - E_{CB}$), the valence band potential (E_{VB}) can be calculated.

$$E_{RHE} = E_{Ag/AgCl} + 0.059\mathrm{pH} + E^{\circ}_{Ag/AgCl} \tag{1}$$

$$E_{NHE} = E_{RHE} - 0.059\mathrm{pH} \tag{2}$$

where $E^{\circ}_{Ag/AgCl} = 0.29\,\mathrm{V}$, pH 5.24.

The E_{CB} was obtained as −0.87, −0.77, and −0.76 V for UiO-66-NH_2, BD2/UiO-66-NH_2, and BD4/UiO-66-NH_2, respectively. Accordingly, the E_{VB} values were calculated to be 1.97,

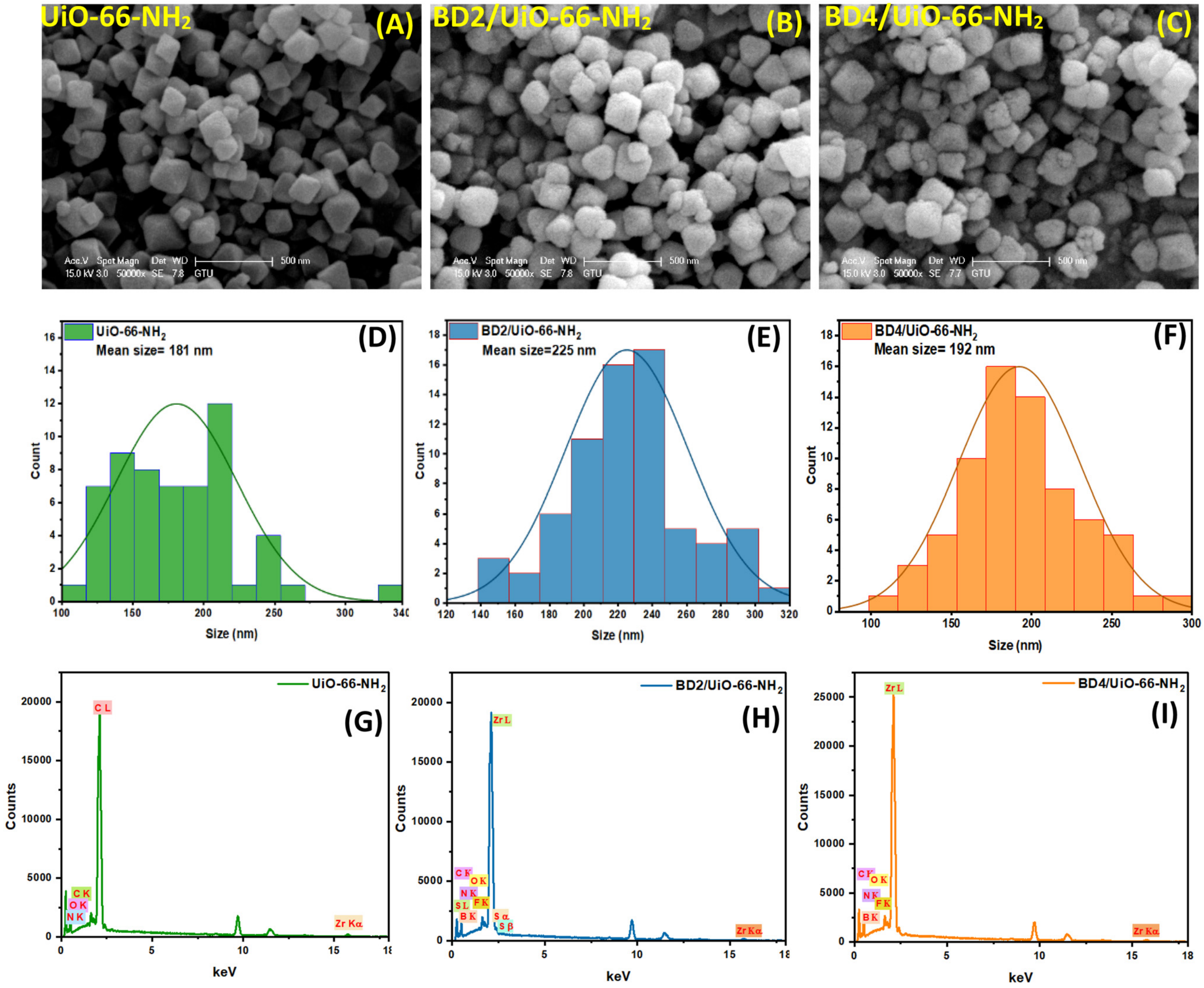

Fig. 3 (A–C) SEM images, (D–F) size distribution graphs, and (G–I) EDS spectrums of the prepared samples.

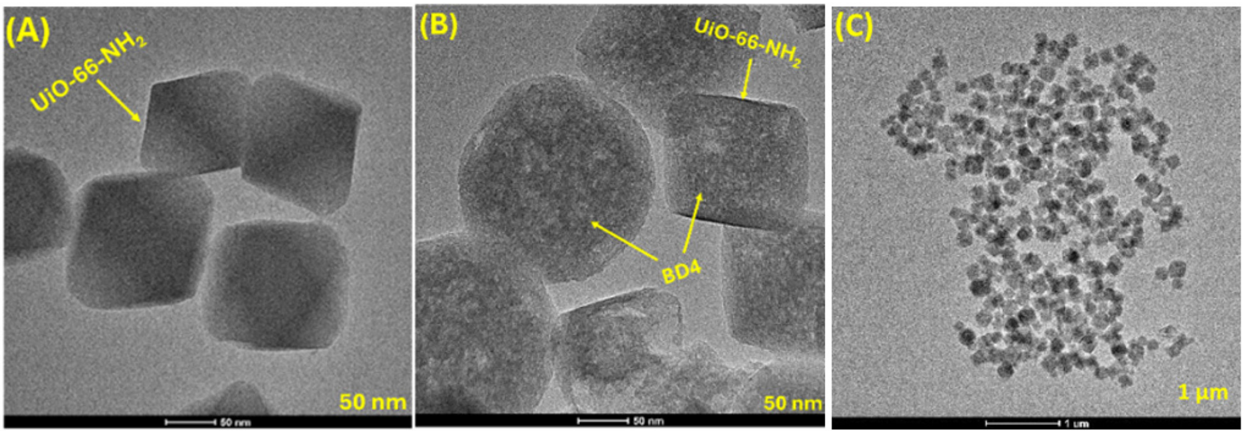

Fig. 4 TEM images of (A) UiO-66-NH$_2$, (B) BD4/UiO-66-NH$_2$ (50 nm), and (C) BD4/UiO-66-NH$_2$ (1 μm).

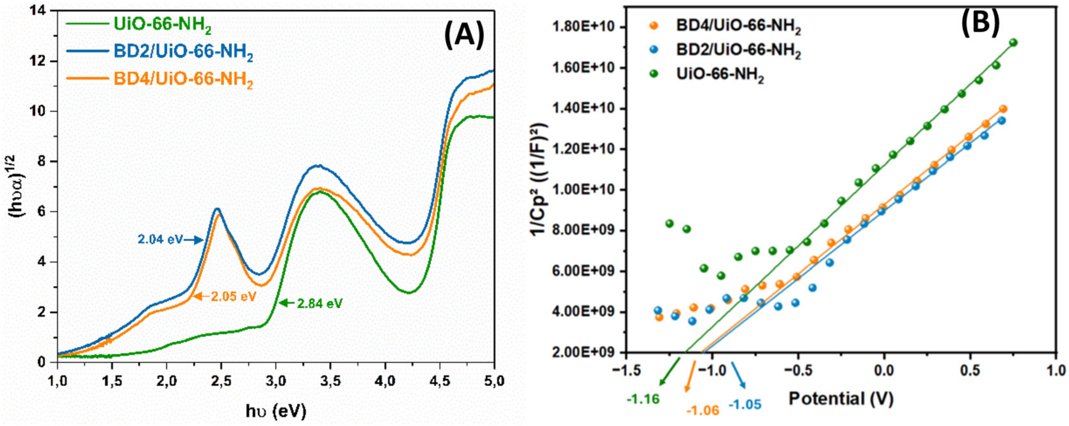

Fig. 5 (A) Tauc plot and (B) Mott–Schottky graphs of the compounds.

1.27, and 1.29 V, respectively, for the same species. The obtained E_{CB} values are more negative than the potential needed for water splitting, which facilitates the hydrogen production in our process.

The electrochemical characterizations of UiO-66-NH_2 and its functionalized derivatives BD2/UiO-66-NH_2 and BD4/UiO-66-NH_2 reveal distinct charge transport and photoelectrochemical behaviors, as shown by the LSV curves (Fig. 6A), photocurrent density measurement (Fig. 6B), EIS Nyquist plots (Fig. 6C), and photocurrent stability test (Fig. 6D). During a cathodic voltage sweep from −0.4 to −1.2 V (Fig. 6A), the bare UiO-66-NH_2 exhibits the highest cathodic current, while BD2

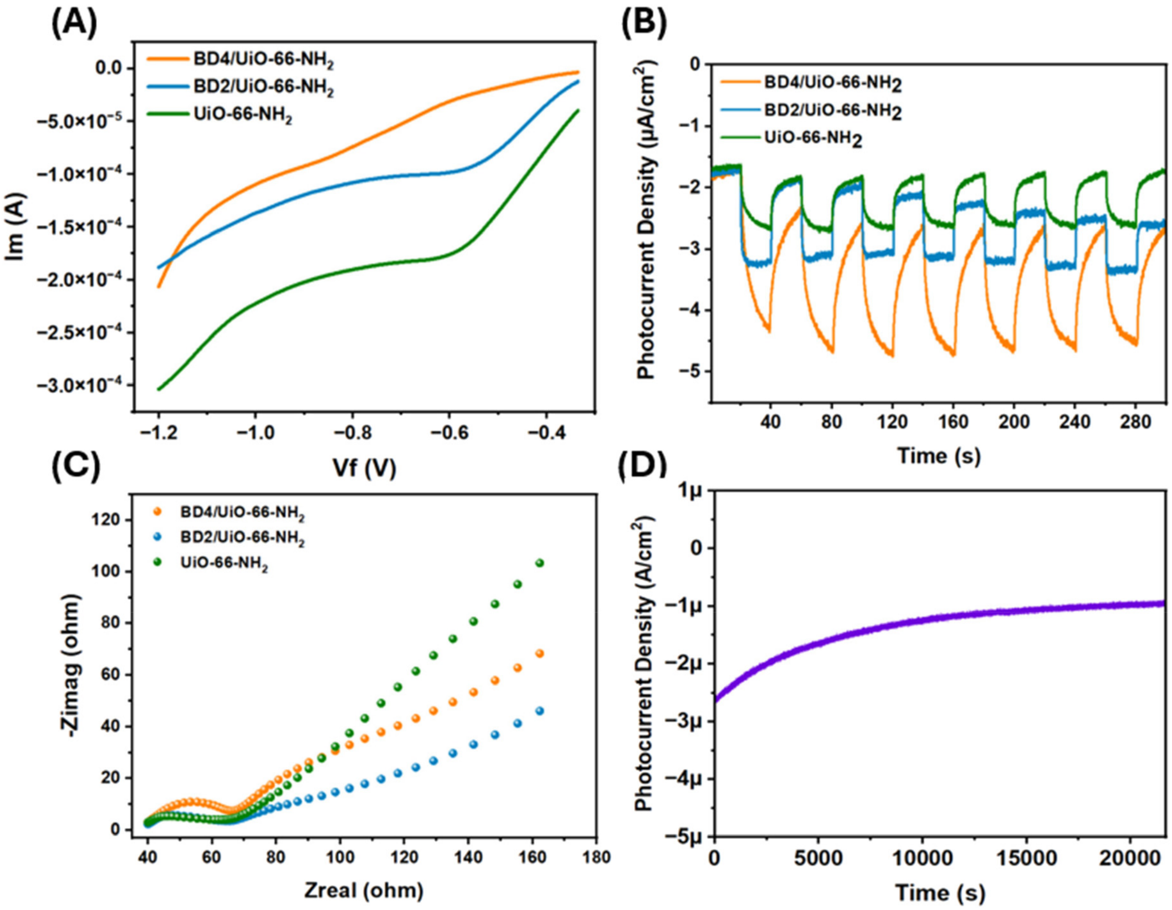

Fig. 6 (A) LSV curves, (B) transient photocurrent density plots, and (C) EIS Nyquist plots of bare and BODIPY-doped UiO-66-NH_2, and (D) photocurrent stability test of BD4/UiO-66-NH_2.

and BD4 functionalization progressively diminishes the observed current magnitudes. This trend initially suggests that BDP functionalization impedes electron transfer or increases charge-transfer resistance, corresponding with the increased impedance shown in the Nyquist plots (Fig. 6C), where functionalized samples exhibit larger semicircle diameters, indicative of elevated charge-transfer resistance relative to that of bare MOF. In contrast, chronoamperometric measurements under intermittent light illumination reveal that both BD2/UiO-66-NH_2 and BD4/UiO-66-NH_2 display significantly enhanced photocurrent densities compared to pristine UiO-66-NH_2 (Fig. 6B). The higher photocurrents for the functionalized materials indicate enhanced photo-induced charge separation and transport efficiency under illumination, which is not fully predicted by their higher intrinsic charge-transfer resistance under dark conditions. This apparent contradiction can be rationalized by considering the distinct mechanisms that control dark electrochemical reduction and photoelectrochemical activity. In Fig. 6A, the dominant processes are electron injection and Faradaic reduction at the electrode interface, where the increased interface resistance and potential structural blocking from the BDP groups reduce the overall current flow. Hence, the functionalized materials demonstrate lower cathodic currents reflecting hindered electron-transfer kinetics in the absence of light excitation. Under illumination (Fig. 6B), however, the attached functional groups likely act as effective photosensitizers or charge mediators. In the case of BD4/UiO-66-NH_2, the phenyl-functionalized BODIPY unit significantly enhances visible-light harvesting and promotes charge separation through an S-scheme mechanism. This synergistic effect produces a higher density of reactive electrons, ensuring that enhanced photogenerated charge kinetics rather than dark interfacial resistance govern the overall hydrogen evolution efficiency (Fig. 6C). The improved photogenerated charge-carrier dynamics surpass the minor resistance increase, demonstrating enhanced photoelectrochemical performance. To evaluate the visible-light stability of BD4/UiO-66-NH_2 (as the species with the best hydrogen evolution potential according to the results obtained from the hydrogen production tests) a long-term stability evaluation was conducted using amperometric *i*–*t* measurements, with the results presented in Fig. 6D. After about 6 hours of continuous operation, no significant change in the photocurrent response was observed, indicating the excellent stability of the BD4/UiO-66-NH_2.

2.1. Photocatalytic hydrogen production

To analyze the hydrogen production potential of the prepared BODIPY-functionalized porous MOF photocatalysts, photocatalytic water-splitting tests were performed. Triethanolamine was used as a sacrificial agent for the tests, and hydrogen evolution rates were measured under solar simulator light irradiation. The photocatalytic H_2 production activity of the synthesized structures from water is compared in Fig. 7. Fig. 7A shows the H_2 evolution results per gram of catalyst as μmol g^{-1}, and Fig. 7B illustrates the hydrogen evolution percentages for each sample. Fig. 7C demonstrates the H_2 generation rates and kinetics of the prepared samples over 1 hour. The reusability of the photocatalyst candidates is one of the most crucial factors in the catalytic process. Therefore, the reusability tests for five-run trials on the most active sample, BD4/UiO-66-NH_2, which shows the best photocatalytic hydrogen evolution capability, were performed, and the results are reported in Fig. 7D. The obtained error bars and the calibration curve with R^2 values for the five-run experiments are given in Fig. 7E and F, respectively. The reproducibility of the results over consecutive cycles indicates the high stability and durability of the BODIPY-modified MOF materials under visible-light irradiation. As given in Fig. 7F, the R^2 value obtained from the average hydrogen evolution measurements over five runs indicates that the synthesized photocatalysts possess a high level of reproducibility. Looking at the amount of H_2 produced, it is observed that the H_2 production capacities of the synthesized structures increased significantly and linearly over 6 hours. The H_2 production potentials of UiO-66-NH_2, BD2/UiO-66-NH_2, and BD4/UiO-66-NH_2 over 6 hours were found to be 18 079 μmol g^{-1}, 85 422 μmol g^{-1}, and 130 674 μmol g^{-1}, respectively. The reaction kinetics at the end of 6 hours were calculated to be 3013 μmol g^{-1} h^{-1}, 14 237 μmol g^{-1} h^{-1}, and 21 179 μmol g^{-1} h^{-1}, respectively. Based on the data obtained, the hydrogen production potential of the MOF structure alone is lower compared to the BODIPY-modified MOFs. The enhanced photocatalytic properties of BODIPY/MOF materials can be attributed to the light-absorbing chromophores present in the materials. Therefore, it can be said that the design of the presented BODIPY/MOFs successfully achieved the goal of enhancing hydrogen production potential. It has been reported that the BODIPY-functionalized MOF structure formed with the thiophene BODIPY compound produced 4.7 times more hydrogen than the MOF structure alone. The structure designed with the phenyl BODIPY compound and MOF demonstrated a 7.2-fold increase in hydrogen-production efficiency. Moreover, to understand the synergy between the BODIPY and MOF structure, the hydrogen evolution kinetics of the pristine BD4 dye were tested and compared with those of BD4/UiO-66-NH_2. The results showed that the HER performance of BD4 alone was 3 times lower than that of the BD4/UiO-66-NH_2. The enhanced performance arises not only from the blending of materials but also from the chemical synergistic interactions between them. Thiophene BODIPY (BD2) substituted MOF enhances π-conjugation and light absorption, giving red-shifted, broader spectra. On the other hand, phenyl BODIPY (BD4) limits conjugation but delivers better photocatalytic performance due to longer-lived excited states, less recombination, stronger reduction potential, and reduced aggregation. Furthermore, the chemical stability of the photocatalyst candidate BD4/UiO-66-NH_2 following the HER reaction was studied with FT-IR, PXRD, and SEM analyses. As illustrated in Fig. S18–S20, the findings indicate that the composite preserves its structural integrity and morphology, with no evidence of degradation. A comparison of SEM images before and after the reaction reveals that, although the overall morphology and particle

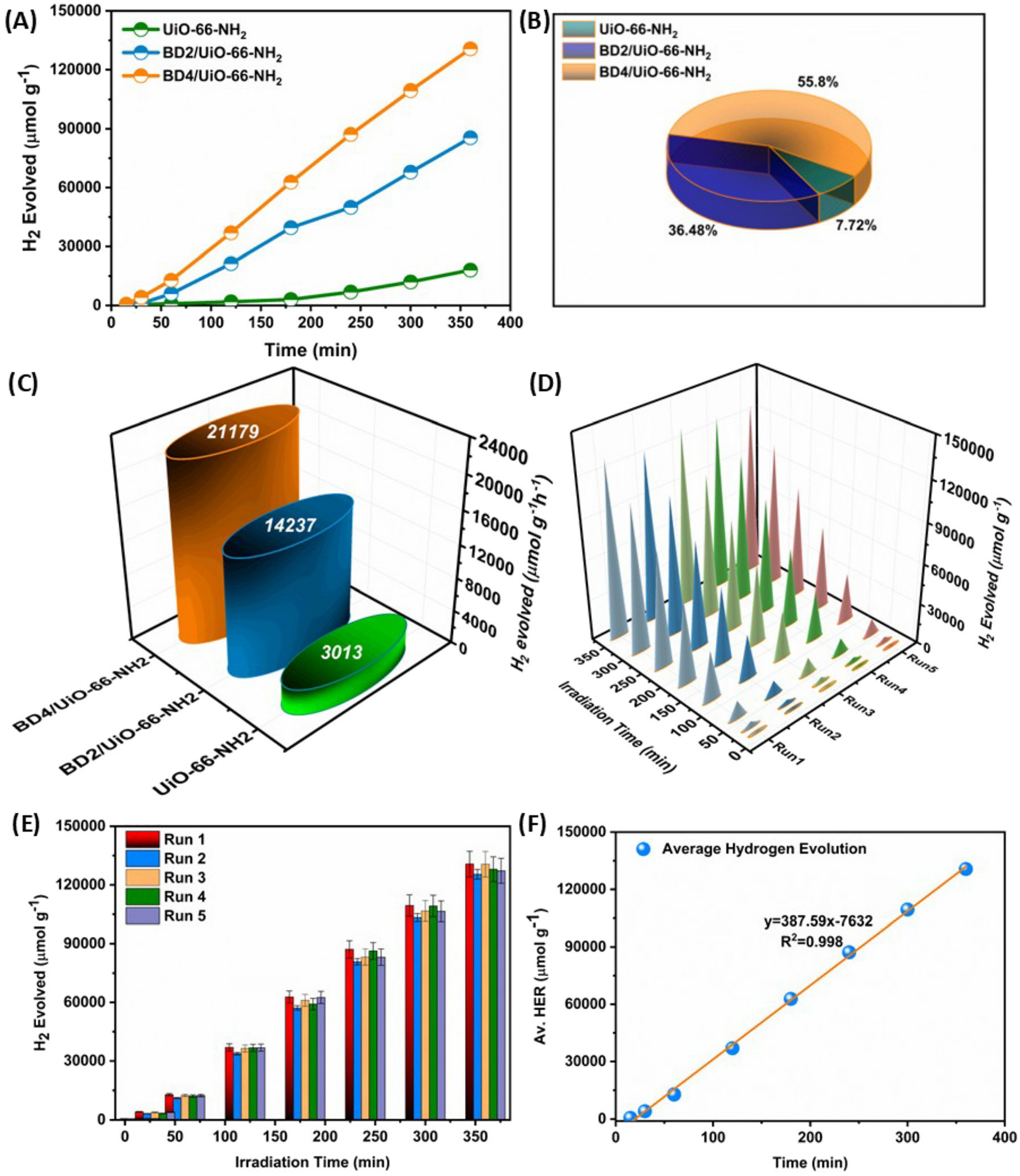

Fig. 7 Amount of hydrogen generated in the photocatalytic water-splitting reaction (A), the corresponding H_2 evolution efficiencies (B), visible-light-driven H_2 production rates (C), the reusability performance of the optimum conjugated polymer (D), Hydrogen evolution amounts with error bars (E), and the Calibration graph of the relation between average H_2 production *versus* time (F).

distribution remain consistent, a reduction in particle size is evident. In parallel, PXRD patterns exhibit no peak shifts, confirming structural stability, although a decrease in peak intensity is observed. Similarly, the FTIR spectra of BD4/UiO-66-NH_2 before and after use show no major changes, confirming the structural stability. The 3000–3500 cm^{-1} band arises from overlapping –NH_2 and –OH vibrations and becomes broader after application due to surface hydroxylation and residual moisture. The unchanged carboxylate peaks at 1500 and 1400 cm^{-1} further indicate that the framework remains intact during water splitting. Considering the results obtained within the scope of the tests, it can be concluded that the prepared BODIPY/MOF structures have high potential as ideal photocatalyst candidates for hydrogen reduction reactions (Table 1).

Yang *et al.* reported the first study on a Pt-decorated BODIPY-based MOF structure (Pt/CCNU) as a photocatalyst candidate for hydrogen production.[25] It was found that the prepared structure achieved a hydrogen evolution rate of

Table 1 Comparison of the visible-light-driven photocatalytic water-splitting activities of MOF and BODIPY-related materials

Photocatalyst type	Sacrificial reagent	Light source	H_2 evolution rate (μmol h^{-1} g^{-1})	Ref.
Pt/CCNU-1	L-Ascorbic acid	Xe lamp $\lambda > 420$ nm	4680 μmol g^{-1} h^{-1}	25
CdS/UiO-66-NH_2	TEOA	Xe lamp-sunlight $\lambda > 320$ nm	64.0 μmol g^{-1} h^{-1}	31
UIO-66-NH_2/covalent triazine-based framework-30NUBC	TEOA	$\lambda > 420$ nm	378 μmol g^{-1} h^{-1}	32
Ti_3C_2/TiO_2/UIO-66-NH_2	Na_2S Na_2SO_3	300 W Xe lamp	1980 μmol g^{-1} h^{-1}	16
$Cd_{0.2}Zn_{0.8}S$@UiO-66-NH_2	Na_2S Na_2SO_3	300 W xenon lamp	5846.5 μmol g^{-1} h^{-1}	33
B-Car/0.75 wt% Pt-TiO_2	Ascorbic acid	Xe lamp (>420 nm filter)	249 μmol g^{-1} h^{-1}	34
BFT-1COOH/Pt@U6N	TEA	$\lambda > 420$ nm	1160 μmol g^{-1} h^{-1}	35
FC-I dirhodium/BODIPY	TEOA	Xenon lamp ($\lambda_{\text{cutoff}} = 420$ nm, 300 W)	275.8 μmol g^{-1} h^{-1}	36
$CU_{0.50}CeO_2$/UiO-66-NH_2	Na_2S Na_2SO_3	300 W xenon lamp ($\lambda_{\text{cutoff}} = 420$ nm)	5662.1 μmol g^{-1} h^{-1}	37
BD4/UiO-66-NH_2	TEOA	Solar simulator	21 179 μmol g^{-1} h^{-1}	Current work

4680 μmol g^{-1} h^{-1} using L-ascorbic acid as a sacrificial agent. The improved photocatalytic performance was attributed to the broad light-absorption ability of the BODIPY unit, the electron-trapping effect of Pt, and the synergism between the individual components. Wang *et al.* reported a photocatalyst candidate that consists of CdS and UiO-66-NH_2 constituents, and the synthesized heterostructure showed greater photocatalytic hydrogen evolution efficiency than that of the bare CdS and MOF, without the need for any co-catalyst, in the presence of TEOA as a sacrificial agent.[31] The improved activity was attributed to the type II mechanism and the synergism exhibited by the components, which facilitates the separation of charge carriers. In another study, Dong *et al.* developed a MOF/COF hybrid composite system and tested its photocatalytic hydrogen evolution efficiency. It was found that the best activity was achieved with 30NUBC with 30% Zr-UiO-66-NH_2 (NU) loading, which is approximately 445-fold higher than that of pure NU and 2-fold greater than that of bare BC COF.[32] The light-absorption ability, electron transfer, and separation of the charge carriers were facilitated by the type II Z-scheme charge-transfer mechanism and the synergistic effect of the components. Tian *et al.* developed a ternary photocatalyst candidate formed with $Ti_3C_2T_x$, TiO_2, and UiO-66-NH_2, and the results revealed that the designed composite has superior photocatalytic hydrogen evolution.[16] The mechanism was depicted as a Schottky junction among the components. Under simulated sunlight, the obtained hybrid structure demonstrated 1980 μmol h^{-1} g^{-1} H_2 evolution, which is greater than that of pure UiO-66-NH_2. The boosted activity resulted from the many interfacial contacts among the components. Due to the interfaces, the separation and transport of the charge carriers were facilitated.

The proposed mechanism behind BODIPY-functionalized UiO-66-NH_2 is presented in Fig. 8. Considering the discussions on the Tauc plot, EIS, photocurrent, and Mott–Schottky analyses, a possible S-scheme mechanism for the composite was proposed. As a result of the band edge positions, UiO-66-NH_2 provides a more negative CB potential (−0.87 eV *vs.* NHE), while BODIPY offers a more positive VB potential (+2.04 eV *vs.* NHE). Therefore, an S-scheme charge-transfer mechanism can be proposed, in which photogenerated electrons in the CB of BODIPY recombine with holes in the VB of UiO-66-NH_2, leaving strongly reducing electrons on the UiO-66-NH_2 CB and strongly oxidizing holes on the BODIPY VB. Furthermore, the Mott–Schottky plots demonstrated that the flat-band potential of pristine UiO-66-NH_2 is −1.16 V, whereas it shifts to −1.06 V upon coupling with BODIPY. This positive shift indicates a decreased electron density and a slight movement of the conduction band edge towards more positive potentials, which can be attributed to interfacial electron transfer from UiO-66-NH_2 to BODIPY and the formation of band bending at the heterojunction. Furthermore, based on literature-derived energy-level estimations, the effective work function of BODIPY dyes is higher than that of UiO-66-NH_2. Accordingly, considering $\Phi \approx 5.37$ eV for BODIPY (estimated from HOMO levels) and $\Phi \approx 5.05$ eV for UiO-66-NH_2 (estimated from the valence band edge), electron transfer is expected to occur from UiO-66-NH_2 to BODIPY upon contact in order to equilibrate their Fermi levels.[38] This electron flow induces downward band bending on the UiO-66-NH_2 side and forms a p-type Schottky-like barrier at the interface. The resulting band arrangement and interfacial electric field support an S-scheme charge-transfer mechanism rather than a simple type-II heterojunction. Under visible-light irradiation, both UiO-66-NH_2 and BODIPY are photoexcited to generate electron–hole pairs. The photogenerated electrons in the CB of BODIPY recombine with the holes in the VB of UiO-66-NH_2 at the interface, forming an S-scheme heterojunction. As a result, highly reducing electrons are preserved in the CB of UiO-66-NH_2, driving the hydrogen evolution reaction ($2H^+ + 2e^- \rightarrow H_2$), while strongly oxidizing holes remain in the VB of BODIPY, which oxidize the sacrificial agent on the oxidation side. Therefore, efficient charge separation and reduced recombination of the electron–hole pairs were enabled, enhancing the overall efficiency.

3. Experimental details

3.1. Materials and methods

All precursors and solvents were sourced from commercial providers. Silica gel plates (Merck, Kieselgel 60 Å, 0.25 mm thick) with the F254 indicator were used for analytical thin-layer

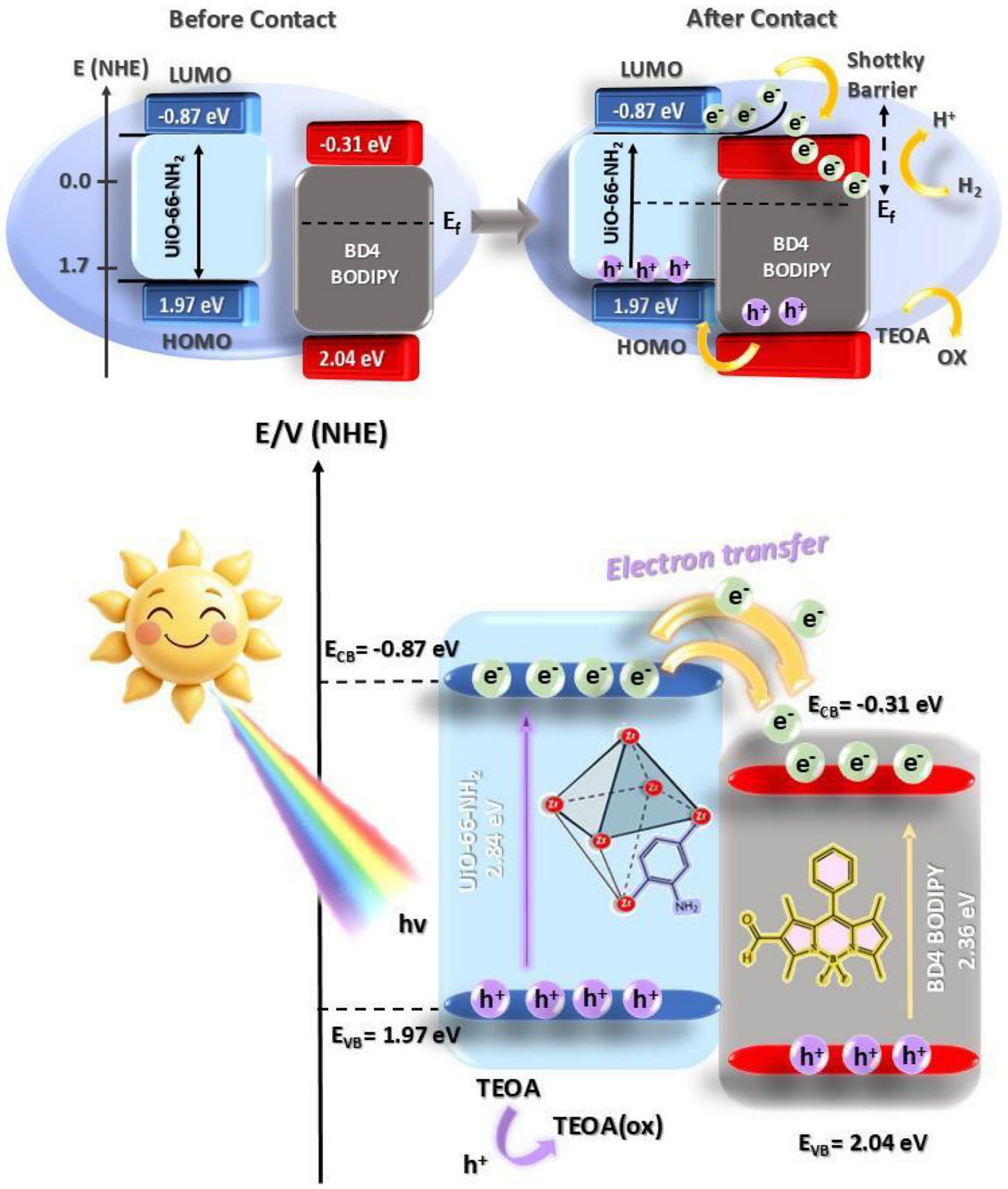

Fig. 8 Schematic overview of energy-band structures and the proposed photocatalytic pathway for the BODIPY/MOFs.

chromatography (TLC) to monitor reaction medium changes. Column chromatography of all products was conducted using silica gel (Merck, Kieselgel 60 Å, 230–400 mesh). Mass spectra were acquired with a Bruker Daltonics microflex mass spectrometer. All NMR spectra (^{1}H and ^{13}C NMR) were recorded on a Varian INOVA 500 MHz spectrometer. FT-IR spectra were recorded between 4000 and 550 cm^{-1} using a Perkin Elmer Spectrum 100 FT-IR spectrometer with attenuated total reflection (ATR). Thermo gravimetric analysis (TGA) was performed on a Mettler Toledo Stare Thermal Analysis System at a heating rate of 10 °C min^{-1} over a temperature range of 25–800 °C under continuous nitrogen flow (50 mL min^{-1}). Powder X-ray diffraction (PXRD) patterns were collected using a Bruker Advanced D8 X-ray diffractometer with Cu Kα (λ = 1.5405 Å) radiation, operated at 30 kV and 30 mA. Scanning electron microscopy (SEM) and energy-dispersive X-ray analysis (EDX) were performed on an FEI (PHILIPS) XL30 SFEG scanning electron microscope. UV-Vis diffuse reflectance spectra

(UV-DRS) were measured using a Shimadzu UV-3600Plus spectrophotometer over 200–1800 nm, with $BaSO_4$ as the reference. Band gap energies were estimated using Tauc plots derived from the Kubelka–Munk transformed spectra. Transmission electron microscopy (TEM) images were captured using an FEI TALOS F200S TEM instrument operated at 200 kV. Photocurrent, electrochemical impedance spectroscopy (EIS), and Mott–Schottky measurements were performed with a Gamry 1010 Electrochemical Analyzer. X-ray photoelectron spectroscopy (XPS) data were obtained with a monochromatic Al Kα radiation source ($h\nu$ = 1486.6 eV) at 15 kV and 150 W under ultrahigh vacuum (~10^{-9} mbar). Calibration of the binding energy scale used the C 1s signal at 284.8 eV. Survey scans ranged from 0 to 1350 eV, with charge compensation applied to reduce surface charging. Data were processed, and peaks were fitted using Shirley background subtraction to account for inelastic scattering. High-resolution spectra were fitted with mixed Gaussian–Lorentzian profiles to represent different chemical states. Hydrogen evolution was analyzed using a Shimadzu gas chromatograph equipped with a thermal conductivity detector and nitrogen as the carrier gas. The nitrogen adsorption–desorption measurements were performed to determine the textural properties of the materials. The surface area and porosity analyses of the pristine UiO-66-NH_2 were conducted using a Micromeritics 3Flex Surface Area and Porosity Analyzer. Before the measurement, the sample was degassed under vacuum at 90 °C for 60 min, followed by a second heating stage at 350 °C for 480 min to ensure the removal of adsorbed species. The analysis was carried out using high-purity nitrogen (N_2) as the adsorbate at 77.210 K. For the functionalized MOF (BD4/UiO-66-NH_2), the analysis was performed on an Anton Paar Autosorb 6100 FKM XR system. The sample was degassed at 130 °C for 1440 min (24 h) prior to analysis. The N_2 adsorption data were collected at an analysis temperature of 77.35 K. For both instruments, the specific surface areas were calculated using the Brunauer–Emmett–Teller (BET) method in the linear relative pressure range.

3.2. Synthesis

BD1, BD3, and UiO-66-NH_2 were prepared according to the literature,[39–41] and the syntheses are described in the SI. The synthesis routes are given in Fig. S1, and ^1H and ^{13}C NMR spectra of BD1 and BD3 are shown in Fig. S2, S3 and Fig. S4, S5, respectively.

3.2.1. Synthesis of BD2. Phosphoryl chloride (3.15 mL, 34.5 mmol) was taken into a double-necked round-bottom flask in an ice bath under an Ar atmosphere, and then, DMF (5.34 mL, 69.0 mmol) was introduced dropwise into the reaction mixture. The resulting solution was maintained under stirring for 5 minutes in an ice bath. Then, it was heated to ambient temperature and stirred for an additional 30 minutes. BD1 (300 mg, 0.69 mmol) in 10 mL of 1,2-dichloroethane was introduced into the reaction flask. Then, the reaction mixture was stirred for 3 hours at room temperature while being monitored by TLC on a silica plate. After the reaction was completed, the mixture was added to ice water, and the pH was adjusted to 7–8 using $NaHCO_3$. The mixture was extracted into DCM, and the organic layer was collected and dried on Na_2SO_4. The solvent of the organic layer was evaporated with a rotary evaporator. The crude product was purified by silica gel column chromatography using DCM as eluent to give BD2 (orange solid, 200 mg, 63%). MALDI TOF (m/z) calc. for $C_{18}H_{17}BF_2N_2OS$: 358.214, found: 358.003 $[M]^+$, 339.631 $[M–F]^+$ (Fig. S6). ^1H NMR (400 MHz, $CDCl_3$) δ_H (ppm): 10.03 (s, 1H, –CHO), 7.56 (m, 1H, Ar–H), 7.24 (m, 1H, Ar–H), 6.99 (m, 1H, Ar–H), 6.16 (s, 1H, Ar–H), 2.81 (s, 3H, $–CH_3$), 2.61 (s, 3H, $–CH_3$), 2.77 (s, 3H, $–CH_3$), 1.56 (s, 3H, $–CH_3$) (Fig. S7). ^{13}C NMR (101 MHz, $CDCl_3$) δ_C (ppm): 162.00, 156.75, 147.49, 143.03, 143.00, 139.14, 134.73, 133.87, 130.21, 128.36, 127.35, 124.34, 124.24, 124.21, 15.34, 14.41, 13.24, 11.16 (Fig. S8).

3.2.2. Synthesis of BD4. Phosphoryl chloride (4.93 mL, 54 mmol) was added to a double-necked round-bottom flask in an ice bath under an Ar atmosphere, then DMF (8.36 mL, 108 mmol) was introduced dropwise to the reaction medium. The resulting mixture was subjected to stirring for 5 minutes in an ice bath. Then, it was heated to ambient temperature and stirred for an additional 30 minutes. BD3 (350 mg, 1.08 mmol) in 10 mL of 1,2-dichloroethane was added to the reaction flask. Then, the mixture was kept under stirring for 3 hours at room temperature, and its progress was tracked using TLC on a silica plate. After the reaction was complete, the acquired mixture was added to ice water, and the pH was adjusted to 7–8 using $NaHCO_3$. Then, DCM was used to extract the mixture, and the organic layer was collected and dried on Na_2SO_4. The solvent of the organic layer was evaporated using a rotary evaporator. Purification of the crude material was achieved using silica gel column chromatography with a 1 : 1 mixture of DCM and *n*-hexane, yielding BD4 (orange solid, 360 mg, 95%). MALDI TOF (m/z) calc. for $C_{20}H_{19}BF_2N_2O$: 352.156, found: 352.042 $[M]^+$, 333.023 $[M–F]^+$ (Fig. S9). ^1H NMR (400 MHz, $CDCl_3$) δ_H (ppm): 10.01 (s, 1H, –CHO), 7.53 (m, 3H, Ar–H), 7.28 (m, 2H, Ar–H), 6.15 (s, 1H, Ar–H), 2.82 (s, 3H, $–CH_3$), 2.62 (s, 3H, $–CH_3$), 1.65 (s, 3H, $–CH_3$), 1.42 (s, 3H, $–CH_3$) (Fig. S10). ^{13}C NMR (101 MHz, $CDCl_3$) δ_C (ppm): 161.85, 156.73, 147.52, 143.78, 143.14, 134.37, 129.77, 129.70, 127.91, 124.21, 15.32, 15.07, 13.25, 11.79 (Fig. S11).[42]

3.2.3. Synthesis of BD2/UiO-66-NH_2. 43 mg of UiO-66-NH_2 and 36 mg of BD2 were placed in a bottle. 2.5 mL of dioxane, 2.5 mL of mesitylene, and 0.5 mL of 6 M acetic acid were introduced to the medium, and the obtained mixture was stirred until a homogeneous mixture was obtained. The mixture was then heated at 120 °C in an oven for a period of 3 days and subsequently cooled to room temperature once the reaction was finished. The product was then purified by washing with DMF, THF, and acetone, and then dried in a 50 °C vacuum oven, yielding a total of 30 mg of solid product (Scheme 1).

3.2.4. Synthesis of BD4/UiO-66-NH_2. To prepare the hybrid material, 43 mg of UiO-66-NH_2 and 36 mg of BD4 were weighed into a suitable reaction vial. 2.5 mL of dioxane, 2.5 mL of mesitylene, and 0.5 mL of 6 M acetic acid were added to this. The mixture was stirred in an ultrasonic bath until a homogeneous solution was formed. The obtained solution was heated in an oven preheated to 120 °C for 72 hours to ensure completion of the reaction. When the reaction was complete, the mixture was cooled to ambient temperature. The resulting solid product was purified by sequentially washing with DMF, THF, and acetone. At the end, the product was dried in a 50 °C vacuum oven to get a total of 30 mg of product (Scheme 1).

3.3. Electrochemical measurements

The electrochemical measurements were done in a three-electrode system, including a reference electrode (Ag/AgCl), counter electrode (Pt), and working electrode (the synthesized compounds). The working electrode was constructed by the electrophoretic deposition of the compounds on FTO glass pieces (measured surface: 1 × 1 cm^2). 0.1 M Na_2SO_4 was used as the electrolyte. The measurements were performed with a Gamry potentiostat interface 1010 E. The electrochemical behavior of the samples was characterized by transient photocurrent density measurements, electrochemical impedance spectroscopy (EIS), Mott–Schottky (MS), and linear sweep voltammetry (LSV). The photo-stability of the prepared electrodes, containing the photocatalysts, was examined by the chronoamperometry method.

3.4. Preparation of the thin films of conjugated polymers

The working electrode that was used for the electrochemical measurements was prepared as follows: a known amount of the synthesized compounds was added to isopropyl alcohol, in the presence of $Mg(NO_3)_2$, and subjected to ultrasonic treatment for 15 min. Then, by applying a DC voltage of 30 V, a thin layer of the photocatalyst was coated on the FTO glass pieces. The prepared films were dried in an oven overnight at 70 °C and were ready to be used the next day.

3.5. Photocatalytic hydrogen evolution experiments

To evaluate the photocatalytic hydrogen evolution performance, experiments were conducted in a 50 mL quartz reactor sealed with a silicone rubber septum. A solar simulator was used as the light source. Typically, 10 mg of each photocatalyst was dispersed in 25 mL of 10% (v/v) triethanolamine (TEOA) aqueous solution under magnetic stirring, serving as a sacrificial agent. Before light irradiation, the solution was purged with nitrogen for 30 minutes to eliminate dissolved oxygen. Hydrogen production was measured using a Shimadzu gas chromatograph equipped with a thermal conductivity detector and nitrogen as the carrier gas, with peak areas recorded periodically in ppm throughout the 6-hour reaction.

4. Conclusions

Although MOF-based photocatalysts incorporating chromophores such as porphyrins, phthalocyanines, and other organic dyes have been extensively studied, BODIPY-based MOF systems remain remarkably scarce. In this study, two new BODIPY/UiO-66-NH_2 nanostructures, containing thiophene and phenyl functional groups, were successfully prepared using the Schiff base reaction. The structural, morphological, optical, and electronic properties of the synthesized materials were elucidated in detail by techniques such as FTIR, XPS, TGA, PXRD, SEM, EDS, TEM, LSV, and EIS. TGA data showed that the integration of bare BODIPY molecules into the MOF backbone significantly improved the low thermal stability that limits the use of BODIPY dyes. This confirmed the successful integration of the BODIPY molecules within the MOF structure. Photocatalytic performance tests strikingly demonstrated the effectiveness of the performed modification. The integration of thiophene- and phenyl-based BODIPY provided 4.7- and 7.2-fold increases in hydrogen production capacity compared to that of the bare UiO-66-NH_2, respectively. These superior performance data prove that the functionalization of UiO-66-NH_2 with BODIPY derivatives positively changes the photoelectronic properties of the material and maximizes the hydrogen production potential. The observed behavior is consistent with an S-scheme charge-transfer pathway, based on the band alignment, photocatalytic performance trends, and indirect supporting evidence.

Overall, this study highlights the unexplored potential of BODIPY–MOF hybrid architectures and establishes a new design concept for efficient, stable, and tunable photocatalysts for sustainable solar-to-hydrogen energy conversion.

Author contributions

Zehra Coşkun: investigation, validation, data curation, writing – original draft. Elif Yıldız Gül: investigation, validation, data curation, writing – original draft. Burcu Topaloğlu Aksoy: investigation, validation, data curation, writing – original draft. Azam Seifi: investigation, validation, data curation, writing – original draft. Esra Tanrıverdi Eçik: conceptualization, methodology, writing – reviewing and editing. Bünyemin Çoşut: methodology, conceptualization, writing – reviewing and editing, supervision.

Conflicts of interest

The authors declare that they have no conflicts of interest in this work.

Data availability

All data obtained during this study are included in this published article and its supplementary information (SI). Supplementary information: details of synthesis and characterization and preparation of experimental procedures for electrochemical and photocatalytic hydrogen evolution. See DOI: https://doi.org/10.1039/d6dt00551a.

Ref. 38–40 are cited in the SI.

Acknowledgements

Dr Bünyemin Çoşut thanks the Turkish Academy of Sciences (TUBA) for support.

References

1 P. A. Owusu and S. Asumadu-Sarkodie, A review of renewable energy sources, sustainability issues and climate change mitigation, *Cogent Eng.*, 2016, **3**(1), 1167990.

2 T. Hisatomi and K. Domen, Reaction systems for solar hydrogen production via water splitting with particulate semiconductor photocatalysts, *Nat. Catal.*, 2019, **2**(5), 387–399.

3 Q. Wang and K. Domen, Particulate Photocatalysts for Light-Driven Water Splitting: Mechanisms, Challenges, and Design Strategies, *Chem. Rev.*, 2020, **120**(2), 919–985.

4 Y. Chen, Q. Tan, Y. Ji, D. Wang, R. Dong and B. Dai, Advancing photocatalysis through efficient fabrication of morphology-engineered photonic crystals, *Inorg. Chem. Front.*, 2025, **12**(20), 5962–5988.

5 K. Maeda and K. Domen, Photocatalytic Water Splitting: Recent Progress and Future Challenges, *J. Phys. Chem. Lett.*, 2010, **1**(18), 2655–2661.

6 L. Han, F. Jing, J. Zhang, X.-Z. Luo, Y.-L. Zhong, K. Wang, *et al.*, Environment friendly and remarkably efficient photocatalytic hydrogen evolution based on metal organic framework derived hexagonal/cubic In2O3 phase-junction, *Appl. Catal., B*, 2021, **282**, 119602.

7 X. Chen, S. Shen, L. Guo and S. S. Mao, Semiconductor-based Photocatalytic Hydrogen Generation, *Chem. Rev.*, 2010, **110**(11), 6503–6570.

8 T. Hisatomi, J. Kubota and K. Domen, Recent advances in semiconductors for photocatalytic and photoelectrochemical water splitting, *Chem. Soc. Rev.*, 2014, **43**(22), 7520–7535.

9 P. Zhou, J. Yu and M. Jaroniec, All-Solid-State Z-Scheme Photocatalytic Systems, *Adv. Mater.*, 2014, **26**(29), 4920–4935.

10 E. Sánchez-González, M. Y. Tsang, J. Troyano, G. A. Craig and S. Furukawa, Assembling metal–organic cages as porous materials, *Chem. Soc. Rev.*, 2022, **51**(12), 4876–4889.

11 J. Zhao, K. Xu, W. Yang, Z. Wang and F. Zhong, The triplet excited state of Bodipy: formation, modulation and application, *Chem. Soc. Rev.*, 2015, **44**(24), 8904–8939.

12 P. De Bonfils, L. Péault, P. Nun and V. Coeffard, State of the Art of Bodipy-Based Photocatalysts in Organic Synthesis, *Eur. J. Org. Chem.*, 2021, **2021**(12), 1809–1824.

13 K. Makino, I. Takuro and Y. Kubo, A benzofuran[b]-fused BODIPY as an efficient sensitizer for photocatalytic hydrogen production, *Sustainable Energy Fuels*, 2021, **5**(14), 3676–3686.

14 M.-S. Lin, Q.-B. Nie, J.-N. Chen, Z.-Y. Liu, Q.-Y. Wu, X.-F. Liu, *et al.*, Synthesis, photophysics and photosensitizing hydrogen evolution of a near-infrared heavy-atom-free sensitizer, *New J. Chem.*, 2025, **49**(18), 7647–7654.

15 L. Zeng, X. Guo, C. He and C. Duan, Metal–Organic Frameworks: Versatile Materials for Heterogeneous Photocatalysis, *ACS Catal.*, 2016, **6**(11), 7935–7947.

16 P. Tian, X. He, L. Zhao, W. Li, W. Fang, H. Chen, *et al.*, Enhanced charge transfer for efficient photocatalytic H2 evolution over UiO-66-NH2 with annealed Ti3C2Tx MXenes, *Int. J. Hydrogen Energy*, 2019, **44**(2), 788–800.

17 J. Zhao, Y. Wang, J. Zhou, P. Qi, S. Li, K. Zhang, *et al.*, A copper(II)-based MOF film for highly efficient visible-light-driven hydrogen production, *J. Mater. Chem. A*, 2016, **4**(19), 7174–7177.

18 V. R. Bakuru, M. E. Dmello and S. B. Kalidindi, Metal-Organic Frameworks for Hydrogen Energy Applications: Advances and Challenges, *ChemPhysChem*, 2019, **20**(10), 1177–1215.

19 H. Li, H. Gong and Z. Jin, Phosphorus modified Ni-MOF–74/BiVO4 S-scheme heterojunction for enhanced photocatalytic hydrogen evolution, *Appl. Catal., B*, 2022, **307**, 121166.

20 K. Berijani and A. Morsali, The role of metal–organic porous frameworks in dual catalysis, *Inorg. Chem. Front.*, 2021, **8**(15), 3618–3658.

21 Y. Wen, Z. Wei, C. Ma, X. Xing, Z. Li and D. Luo, MXene Boosted CoNi-ZIF-67 as Highly Efficient Electrocatalysts for Oxygen Evolution, *Nanomaterials*, 2019, **9**(5), 775.

22 D. Bai, F. Chen, D. Jiang and Y. He, A rare Pb9 cluster-organic framework constructed from a flexible cyclotriphosphazene-functionalized hexacarboxylate exhibiting selective gas separation, *Inorg. Chem. Front.*, 2017, **4**(9), 1501–1508.

23 M. Yi, F. Héraly, J. Chang, A. K. Kheirabad, J. Yuan, Y. Wang, *et al.*, A transport channel-regulated MXene membrane via organic phosphonic acids for efficient water permeation, *Chem. Commun.*, 2021, **57**(51), 6245–6248.

24 S. Pullen and S. Ott, Photochemical Hydrogen Production with Metal–Organic Frameworks, *Top. Catal.*, 2016, **59**(19–20), 1712–1721.

25 H. Yang, J. Wang, J. Ma, H. Yang, J. Zhang, K. Lv, *et al.*, A novel BODIPY-based MOF photocatalyst for efficient visible-light-driven hydrogen evolution, *J. Mater. Chem. A*, 2019, **7**(17), 10439–10445.

26 C. Y. Lee, O. K. Farha, B. J. Hong, A. A. Sarjeant, S. T. Nguyen and J. T. Hupp, Light-Harvesting Metal–Organic Frameworks (MOFs): Efficient Strut-to-Strut Energy Transfer in Bodipy and Porphyrin-Based MOFs, *J. Am. Chem. Soc.*, 2011, **133**(40), 15858–15861.

27 A. Atilgan, T. Islamoglu, A. J. Howarth, J. T. Hupp and O. K. Farha, Detoxification of a Sulfur Mustard Simulant Using a BODIPY-Functionalized Zirconium-Based Metal–Organic Framework, *ACS Appl. Mater. Interfaces*, 2017, **9**(29), 24555–24560.

28 M. Pourkhosravani, S. Dehghanpour, F. Farzaneh and S. Sohrabi, Designing new catalytic nanoreactors for the regioselective epoxidation of geraniol by the post-synthetic immobilization of oxovanadium(IV) complexes on a ZrIV-based metal–organic framework, *React. Kinet., Mech. Catal.*, 2017, **122**(2), 961–981.

29 C. Wu and H. Y. Almuaalemi, Synthesis of MOFs and Characterization and Drug Loading Efficiency, *ChemEngineering*, 2025, **9**(2), 24.

30 C. F. Holder and R. E. Schaak, Tutorial on Powder X-ray Diffraction for Characterizing Nanoscale Materials, *ACS Nano*, 2019, **13**(7), 7359–7365.

31 Y. Wang, L. Gudiño, J. Bedia and C. Belver, Solar photocatalytic hydrogen production through metal sulfide/UiO-66-NH2 heterojunctions, *Sep. Purif. Technol.*, 2025, **353**, 128663.

32 S. Dong, X. Liu, X. Kong, F. Dong, Y. Yu, L. Wang, *et al.*, Boosting photocatalytic H2 evolution on UIO-66-NH2/covalent triazine–based frameworks composites by constructing a covalent heterojunction, *Environ. Sci. Pollut. Res.*, 2023, **30**(51), 111039–111050.

33 Y. Su, Z. Zhang, H. Liu and Y. Wang, Cd0.2Zn0.8S@UiO-66-NH2 nanocomposites as efficient and stable visible-light-driven photocatalyst for H2 evolution and CO2 reduction, *Appl. Catal., B*, 2017, **200**, 448–457.

34 X.-F. Shen, M. Watanabe, A. Takagaki, J. T. Song and T. Ishihara, Pyridyl-Anchored Type BODIPY Sensitizer-TiO2 Photocatalyst for Enhanced Visible Light-Driven Photocatalytic Hydrogen Production, *Catalysts*, 2020, **10**(5), 535.

35 Q.-Z. Chen, X.-A. Li, Z.-Z. Liang, X.-b. Peng, P.-Y. Su and J.-M. Liu, Molecular Engineering of Calixarene Dyes on UiO-66-NH2: Boosting Electron Transfer for High-Efficiency Photocatalytic Hydrogen Evolution, *Langmuir*, 2025, **41**(32), 21790–21799.

36 P. Chinapang, H. Iwami, T. Enomoto, T. Akai, M. Kondo and S. Masaoka, Dirhodium-Based Supramolecular Framework Catalyst for Visible-Light-Driven Hydrogen Evolution, *Inorg. Chem.*, 2021, **60**(17), 12634–12643.

37 H. Zhang, Y. Wan, S. Shang, Q. Cheng and Z. Pan, Construction of a direct Z-scheme CeO_2/UiO-66-NH2 heterojunction for boosting photocatalytic organic pollutant degradation and H2 evolution performance, *Dalton Trans.*, 2023, **52**(14), 4562–4573.

38 A. Loudet and K. Burgess, BODIPY Dyes and Their Derivatives: Syntheses and Spectroscopic Properties, *Chem. Rev.*, 2007, **107**(11), 4891–4932.

39 T. Jun, K. Kim, K. M. Lee, A. C. Benniston and D. G. Churchill, Meso-thienyl and furyl rotor effects in BF2-chelated dipyrrin dyes: solution spectroscopic studies and X-ray structural packing analysis of isomer and congener effects, *J. Coord. Chem.*, 2012, **65**(24), 4299–4314.

40 C. Duan, Y. Zhou, G.-G. Shan, Y. Chen, W. Zhao, D. Yuan, *et al.*, Bright solid-state red-emissive BODIPYs: facile synthesis and their high-contrast mechanochromic properties, *J. Mater. Chem. C*, 2019, **7**(12), 3471–3478.

41 M. Kandiah, M. H. Nilsen, S. Usseglio, S. Jakobsen, U. Olsbye, M. Tilset, *et al.*, Synthesis and Stability of Tagged UiO-66 Zr-MOFs, *Chem. Mater.*, 2010, **22**(24), 6632–6640.

42 R. C. R. Gonçalves, F. Teixeira, P. Peñalver, S. P. G. Costa, J. C. Morales and M. M. M. Raposo, Designing Antitrypanosomal and Antileishmanial BODIPY Derivatives: A Computational and In Vitro Assessment, *Molecules*, 2024, **29**(9), 2072.